Progenitor Constraint with Circumstellar Material for the Magnetar-hosting Supernova Remnant RCW 103

Takuto Narita[1] , Hiroyuki Uchida[1] , Takashi Yoshida[2] , Takaaki Tanaka[3] , and Takeshi Go Tsuru[1]
[1] Department of Physics, Kyoto University, Kitashirakawa Oiwake-cho, Sakyo, Kyoto, 606-8502, Japan; narita.takuto.l07@kyoto-u.jp
[2] Yukawa Institute for Theoretical Physics, Kyoto University, Kitashirakawa Oiwake-cho, Sakyo, Kyoto 606-8502, Japan
[3] Department of Physics, Konan University, 8-9-1 Okamoto, Higashinada, Kobe, Hyogo 658-8501, Japan

Abstract

Stellar winds blown out from massive stars ($\gtrsim 10\ M_\odot$) contain precious information on the progenitor itself, and in this context the most important elements are carbon (C), nitrogen (N), and oxygen (O), which are produced by the CNO cycle in the H-burning layer. Although their X-ray fluorescence lines are expected to be detected in swept-up shock-heated circumstellar materials in supernova remnants, those of C and N have been particularly difficult to detect so far. Here, we present high-resolution spectroscopy of the young magnetar-hosting supernova remnant RCW 103 with the Reflection Grating Spectrometer on board XMM-Newton and report on the detection of the N VII Lyα (0.50 keV) line for the first time. By comparing the obtained abundance ratio of N to O (N/O = 3.8 ± 0.1) with various stellar evolution models, we show that the progenitor of RCW 103 is likely to have a low mass (10–12 $M_\odot$) and medium rotation velocity ($\lesssim 100\ \mathrm{km\ s^{-1}}$). The results also rule out the possibility of dynamo effects in massive ($\geqslant 35\ M_\odot$) stars as a mechanism for forming the associated magnetar 1E 161348−5055. Our method is useful for estimating various progenitor parameters for future missions with microcalorimeters such as XRISM and Athena.

1. Introduction

Circumstellar material (CSM) around core-collapse (CC) supernova remnants (SNRs) provides us with important clues to understanding their progenitors (e.g., Dwarkadas 2005, 2007; Sapienza et al. 2022), particularly for massive stars ($\gtrsim 10\ M_\odot$; Smartt 2009). This is because elemental abundances in the CSM directly reflect the physical conditions of progenitors: e.g., zero-age main-sequence mass (M_{ZAMS}), initial rotation velocity, and the effects of convective overshoot (Maeder et al. 2014). In this context, lighter elements, such as nitrogen (N), oxygen (O), and carbon (C), are the most critical since they are produced by the CNO cycle in the H-burning layer. Among them, N is produced by consuming C and O (e.g., Maeder 1983), and then is mixed to the star's surface by convection and centrifugal force (e.g., Przybilla et al. 2010). Since N-rich materials are blown out by radiation pressure at the stage of red supergiants (RSGs) and/or Wolf–Rayet stars (WRs) (e.g., Owocki 2004), abundance ratios of N to O (N/O) and N to C (N/C) in the CSM are ideal probes to constrain the progenitors of CC SNRs.

While the CNO elements contain fruitful information on progenitors, it is technically difficult to detect their X-ray fluorescence lines in the soft bands (below ∼0.5 keV; especially C and N) due to the lack of sensitivity and energy resolution of current detectors. For estimating M_{ZAMS} and explosion energies of SNRs, many previous studies have alternatively focused on abundances of magnesium (Mg), silicon (Si), sulfur (S), and iron (Fe) in ejecta (see Sukhbold et al. 2016; Katsuda et al. 2018) since their fluorescence lines are commonly dominant in SNRs. Several observations of Galactic SNRs, however, enable detection of C VI Lyα (0.36 keV) and N VII Lyα (0.50 keV) by

using the Reflection Grating Spectrometer (RGS) on board XMM-Newton (e.g., Uchida et al. 2019; Kasuga et al. 2021). They targeted clumpy structures to avoid degrading the energy resolution of the grating spectrometer. This method will become useful when we attempt to measure abundances of the CNO elements contained in CSM.

Here we focus on a young Galactic CC SNR, RCW 103, which has a clumpy X-ray morphology and hosts the magnetar candidate 1E 161348−5055. The age of the remnant is estimated to be around 2000 yr by comparing an optical image with a photographic plate (Carter et al. 1997) and the distance is estimated to be 3.1 kpc from the systemic velocity of the H I line (Reynoso et al. 2004). While the origin of 1E 161348−5055, which shows an extremely long periodicity (6.67 hr; De Luca et al. 2006), is currently unknown, the progenitor M_{ZAMS} of RCW 103 is also controversial: 18 $M_\odot$ (Frank et al. 2015), 12–13 $M_\odot$ (Braun et al. 2019), or <13 $M_\odot$ (Zhou et al. 2019), which are derived from abundance patterns of the ejecta.

In this paper, we investigate a CSM-dominant outer region of RCW 103 (Sections 2 and 3) and estimate physical conditions of progenitors, such as M_{ZAMS} and the initial rotation velocity (Sections 4.1 and 4.3). We also discuss the relation between the progenitor star and the formation process of the magnetar 1E 161348−5055 in Section 4.4 and summarize our conclusions in Section 5. Throughout the paper, the age and distance of RCW 103 are assumed to be 2000 yr (Carter et al. 1997) and 3.1 kpc (Reynoso et al. 2004). Errors of parameters are defined as 1σ confidence intervals.

2. Observations

RCW 103 was observed with XMM-Newton four times as listed in Table 1. For the following analysis, we only used the RGS and the European Photon Imaging Camera (EPIC) data of these observations. A nearby blank-sky observation
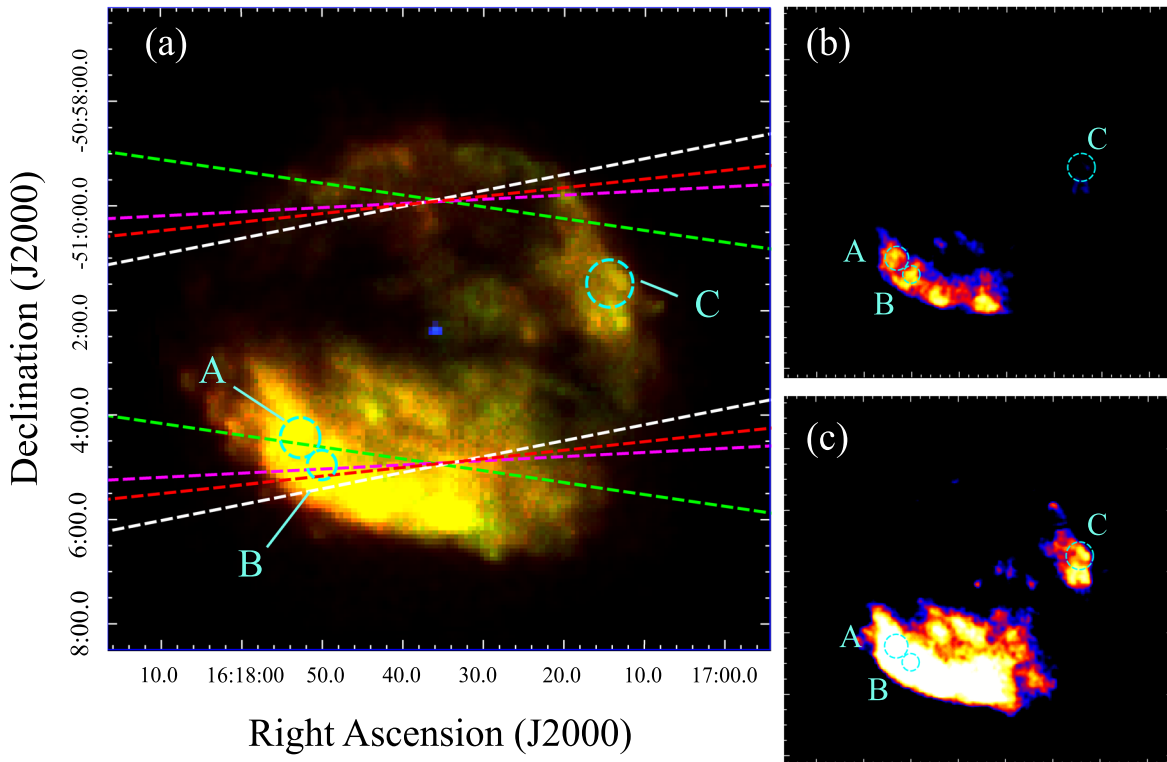
Figure 1. (a) True-color image of RCW 103 from the MOS1+MOS2 data taken in 2001. Red, green, and blue correspond to the energy bands 0.40–0.75 keV, 0.75–1.3 keV, and 2.0–7.2 keV, respectively. The dashed lines represent the cross-dispersion widths of the RGS (5′) and the color of the line corresponds to observation IDs 0113050601 (white), 0302390101 (red), 0743750201 (green), and 0805050101 (magenta). Dashed cyan circles represent the spectral extraction regions. (b) Soft-band image of RCW 103 (0.5–1.2 keV). (c) The same as panel (b) but the color scale is different to clarify a faint structure in region C.

Table 1
Observation Data

	Observation ID	Starting Time	Effective Exposure Time (ks)			
			MOS1	MOS2	RGS1	RGS2
RCW 103	0113050601	2001 Sep 3	13.2	14.1	9.9	9.6
	0302390101	2005 Aug 23	54.5	56.5	58.7	58.6
	0743750201	2016 Aug 19	…	…	49.7	48.8
	0805050101	2018 Feb 14	55.7	57.4	35.6	35.1
Background	0113050701	2001 Sep 3	10.7	11.0	11.0	10.7

(see Table 1) was applied for estimating the background emission. Since the pn-CCD camera was operated in the small-window mode throughout the observation and did not cover the shell regions of the SNR, we did not use the pn data in our analysis. The data from the metal oxide semiconductor (MOS) cameras taken in 2006 were also eliminated for the same reason.

The MOS event files were processed using the pipeline tool `emchain` in version 18.0.0 of the XMM-Newton Science Analysis System (SAS). The RGS data were processed with the RGS pipeline tool `rgsproc` in SAS. We obtained total exposure times as summarized in Table 1 after removing background flares according to the screening with the standard event selection criteria.

3. Analysis and Results

As shown in the soft-band (0.5–1.2 keV) image of RCW 103 (Figure 1), the remnant has bright shells in the southeast and northwest, where CSM is thought to be swept up by forward shocks (see Frank et al. 2015). We selected three compact bright knots in the shells (regions A, B, and C; see Figure 1) so that we

can get high energy resolution with the RGS. The angular size of each region is roughly ≲1′, which is enough to resolve CNO lines. From the obtained RGS spectrum shown in Figure 2, we detected several fluorescence lines below 1 keV. Among them, it is notable that a strong emission line of N^{6+} (N VII Lyα at 0.50 keV) was clearly identified for the first time in RCW 103.

For the following spectral analysis, we used version 12.11.1 of the XSPEC software (Arnaud 1996), in which we use the maximum likelihood W-statistic (Wachter et al. 1979). We combined the RGS data (RGS1+2) and simultaneously fitted first/second-order RGS and MOS spectra. Soft (≲1 keV) and full (≲5 keV) energy bands were used for the RGS and MOS, respectively. We modified RGS response matrices (RMFs) so as to take into account the spatial degradation of the resolution with `rgsrmfsmooth` in FTOOL. Since each line image has a different spatial distribution (Figure 3), we applied different RMFs to each line band.

Previous studies (Frank et al. 2015; Braun et al. 2019; Zhou et al. 2019) report that the X-ray emission of RCW 103 generally originates from both shock-heated ejecta and CSM (or
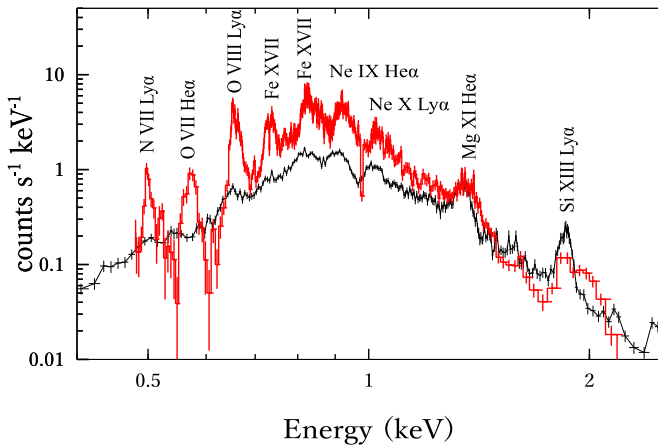
Figure 2. MOS and first-order RGS spectra of region A observed in 2001. The red lines and points represent the RGS data whereas black represents MOS1 data.

in some cases interstellar medium, ISM). We therefore applied an absorbed two-component nonequilibrium ionization (NEI) model with variable abundance in XSPEC: `tbabs*(vnei +vnei)`, where `tbabs` represents the Tübingen–Boulder interstellar absorption (Wilms et al. 2000). The hydrogen column density (N_H) was allowed to vary. Free parameters of the NEI components were the electron temperature (kT_e), ionization timescale ($n_e t$, where n_e is the electron number density and t is the elapsed time since ionization started), and normalization. The abundances of Ne, Mg, Si, S, and Fe (= Ni) for the hot component and those of N, O, and Ne for the cold component were set free, whereas the others were fixed at solar values (Wilms et al. 2000).

We note that the above model cannot represent line-like residuals found at ~1.2 keV, which has often been pointed out by previous SNR studies using the NEI model (see Okon et al. 2020). They suggest that it is attributed to an uncertainty in emissivity data of Fe–L lines, or to physical processes such as charge exchange that are not taken into account in the model. According to their method, we added a Gaussian component at 1.23 keV and found that the fit was improved (W-statistics value/d.o.f.: 20,852/15,341 to 20,769/15,339 for region A) without any significant change of the other parameters. We thus applied the two-component NEI model with a single Gaussian for the following analysis.

Figure 4 shows fits of the two-component NEI model to the spectra. The best-fit parameters are listed in Table 2. The values of N_H and parameters for the high-kT_e component are consistent with the ejecta abundance measured by previous studies (Frank et al. 2015; Braun et al. 2019; Zhou et al. 2019). We find that there is no significant difference among the three regions in the abundances of the low-kT_e component. The abundance of N particularly exceeds the solar value in at least two regions. On the other hand, those of O and Ne are significantly lower than solar. These results suggest that the detected N and O lines originate from the shock-heated CSM blown off by the progenitor's stellar wind.

4. Discussion

4.1. Evidence of CSM and its Composition

While it is expected that CSM contains N-rich materials produced in stars (e.g., Maeder 1983) and that the resultant N/O

becomes higher than solar, it has been difficult to detect N lines in SNRs so far. Frank et al. (2015) found that the plasmas in the shell of RCW 103 have subsolar (~0.5) abundances of heavier elements (Ne, Mg, Si, S, and Fe) and presumed that the CSM is a largely dominant component across the remnant. Our result confirms their conclusion and shows robust evidence of the N-rich shell in RCW 103 for the first time. The averaged abundance ratio is N/O = 3.8 ± 0.1, which fits well into the picture in which the N-rich materials yielded from a massive star are blown out at the RSG or WR stage (e.g., Owocki 2004).

On the basis of this result, we constrain environments around the progenitor of RCW 103 in its pre-supernova phase, where stellar winds are blown out with various abundances in various conditions. As illustrated in Figure 5, we assume two cases with different CSM structures, in which we take into account CSM-hydrodynamic and stellar evolutions as described below. The region furthest from a central star is called a main-sequence (MS) shell and contains MS winds and swept-up ISM (Weaver et al. 1977). The region inside the MS shell is called a stellar wind bubble and is formed by shock waves through collision between the MS winds and the ISM (Castor et al. 1975).

When the wind bubble comes into pressure equilibrium with surroundings, its radius r_{wb} is given by

$$r_{wb} = 5.8 \left(\frac{M_w}{10^{-2} M_\odot} \right)^{1/3} \left(\frac{v_w}{700 \text{ km s}^{-1}} \right)^{2/3}$$
$$\times \left(\frac{p_i/k}{10^4 \text{ cm}^{-3} \text{ K}} \right)^{-1/3} \text{ pc,} \qquad (1)$$

where M_w and v_w are the total mass and velocity of the MS wind, respectively. The value p_i is the pressure of ISM, and k is Boltzmann's constant (Chevalier 1999). In our Galaxy, p_i/k and v_w at the MS are typically $\sim 10^4$ cm^{-3} K (e.g., Berghöfer et al. 1998) and $\sim 10^3$ km s^{-1}, respectively (as summarized by Chen et al. 2013). Since the total wind mass M_w depends on the progenitor mass M_{ZAMS}, we calculated a typical value using a stellar evolution code (Hongo Stellar Hydrodynamics Investigator, HOSHI) developed by Takahashi et al. (2013, 2014, 2016, 2018) and Yoshida et al. (2019). As a result, if the progenitor has M_{ZAMS} of 10 $M_\odot$, the obtained wind mass is $M_w = 9.5 \times 10^{-1} M_\odot$. In this condition, the radius of the wind bubble r_{wb} is calculated as

$$r_{wb}|_{M_{ZAMS}=10M_\odot} = 15.6 \left(\frac{M_w}{9.5 \times 10^{-1} M_\odot} \right)^{1/3}$$
$$\times \left(\frac{v_w}{10^3 \text{ km s}^{-1}} \right)^{2/3} \left(\frac{p_i/k}{10^4 \text{ cm}^{-3} \text{ K}} \right)^{-1/3} \text{ pc.} \qquad (2)$$

Since the size of the wind bubble has a positive liner relation with M_{ZAMS} (Chen et al. 2013), Equation (2) gives a minimum value of r_{wb} by assuming a lower limit $M_{ZAMS} \sim 10 M_\odot$ for CC SN progenitors. On the other hand, RCW 103 has a radius of 4.5 pc (see Figure 5), which confirms that the bright clumps observed in our study are within the MS wind shell; the low-kT_e component is not contaminated by ISM.

To investigate the abundance pattern of the swept-up CSM, the stellar wind blown out just before the SN explosion is the most important component. Stars of relatively low M_{ZAMS} end up as RSGs surrounded by an RSG wind (Figure 5(a)), whose
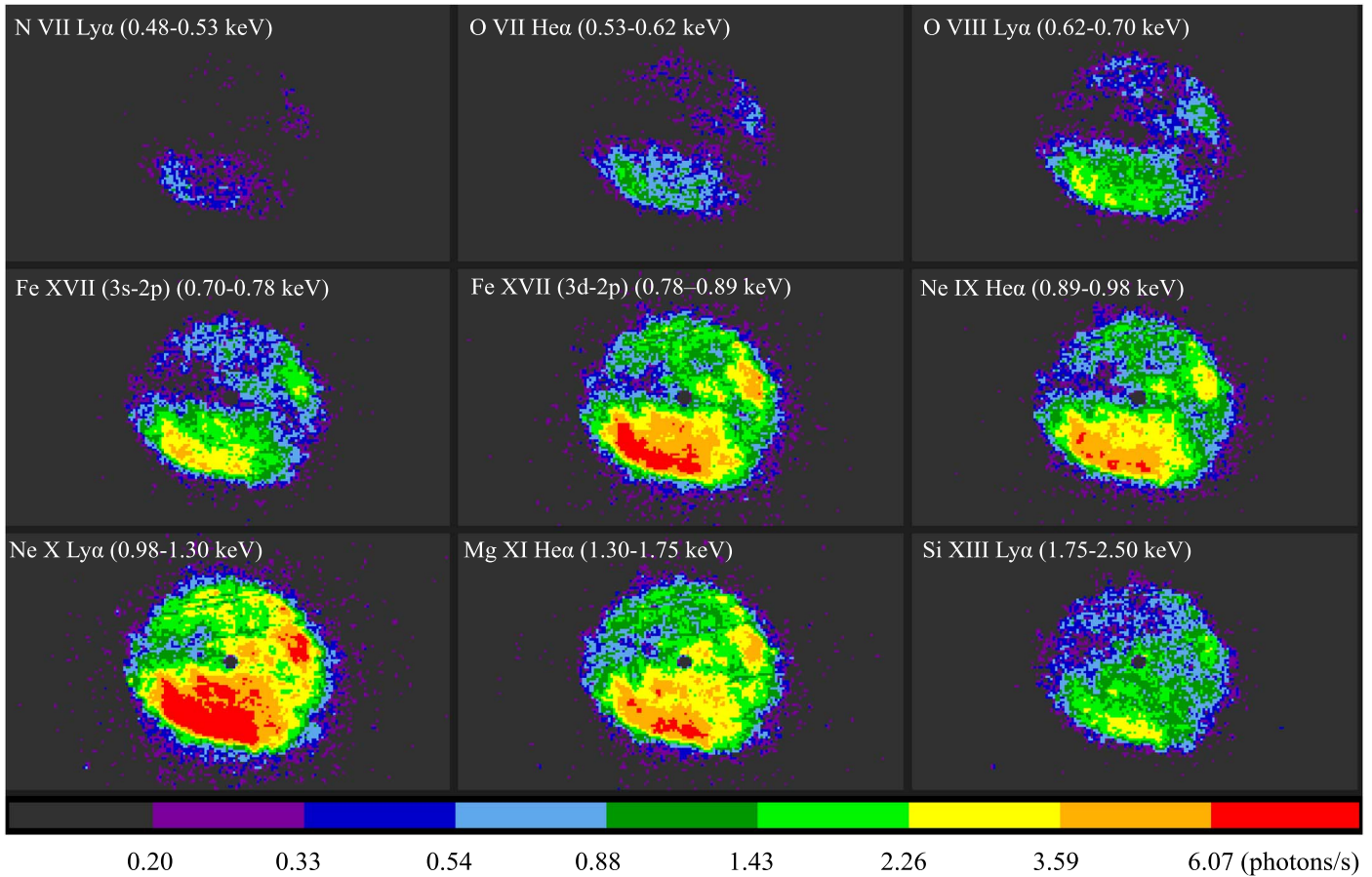
Figure 3. MOS1 images showing the brightness distribution of each emission line labeled in Figure 2. The central region, where the bright magnetar is located, is masked for display.

radius r_{RSG} is described as

$$r_{RSG} \leqslant 2.6 \left(\frac{\dot{M}_w}{5 \times 10^{-7} \, M_\odot \, \mathrm{yr}^{-1}} \right)^{1/2} \left(\frac{v_w}{15 \, \mathrm{km \, s^{-1}}} \right)^{1/2}$$

$$\times \left(\frac{p_{wb}/k}{10^4 \, \mathrm{cm}^{-3} \, \mathrm{K}} \right)^{-1/2} \mathrm{pc}, \qquad (3)$$

where $\dot{M}_w$ and v_w are the mass-loss rate and velocity of the RSG wind, respectively. The value p_{wb} represents the pressure of stellar wind bubbles (Chevalier & Emmering 1989; Chevalier 2005). In Equation (3), we assume a typical pressure of bubbles $\sim 10^4 \, \mathrm{cm}^{-3} \, \mathrm{K}$ (Castor et al. 1975), wind velocity at the RSG phase 10–20 km s^{-1} (Goldman et al. 2017), and the mass-loss rate $\sim 10^{-5}$–$10^{-7} \, M_\odot \, \mathrm{yr}^{-1}$ calculated with the HOSHI code. The result indicates that the swept-up CSM in RCW 103 contains all RSG wind materials if the progenitor ended up as an RSG.

If the progenitor of RCW 103 was a high-M_{ZAMS} star, we additionally need to consider the effect of the WR wind, which may sweep up the ambient RSG wind material before the SN explosion. The WR wind expands into the RSG wind materials with a velocity of 100–200 km s^{-1} (Chevalier & Imamura 1983; Chevalier 2005) during a WR phase of duration $\sim 10^3$–10^4 yr for $M_{ZAMS} \leqslant 60 \, M_\odot$ (from a calculation using the stellar evolution model Geneva Code, Ekström et al. 2012). From these estimations, the radius of the shell of the RSG wind swept up by the WR wind is calculated to be $\leqslant 2.5$ pc. The bright clumps

therefore contain all the RSG and WR materials if the progenitor of RCW 103 ended up as a WR star (Figure 5(b)).

4.2. Stellar Wind History of the Progenitor

To constrain progenitors, we need to know the relationship between CSM abundances and the conditions of stars. The N/O ratio measured in CSM is related to the progenitor M_{ZAMS}, rotation velocity (Maeder et al. 2014), and convective overshoot (the extension of convective motion due to nonzero velocities of material on the boundary between the convection zone and the radiative zone in stars). We therefore investigate trends between N/O and progenitor parameters by using the HOSHI code. The results are summarized in Figure 6. Note that in our calculation, the metallicity, which may also affect our study (Maeder et al. 2014), is assumed to be solar since RCW 103 is a young Galactic SNR. As shown in Figure 6, N/O increases at the stellar surface during the evolution, but its timescale depends strongly on the assumed stellar properties.

M_{ZAMS} is generally thought to have a positive relationship with N/O since the mass-loss rate is positively related to M_{ZAMS} (e.g., Mauron & Josselin 2011). Figures 6(b1) and (c1) indicate that a more rapid increase of N/O is expected in case of higher M_{ZAMS}. This is because a subsolar outer layer (N/O ~ 1) is blown out in an early stage of evolution due to the higher mass-loss rate caused by a stronger radiative force (e.g., Mauron & Josselin 2011). In contrast, lower-mass progenitors ($M_{ZAMS} \leqslant 12 \, M_\odot$) result in a rapid increase of N/O at an earlier stage of stellar evolution. This is possibly because N-rich materials in
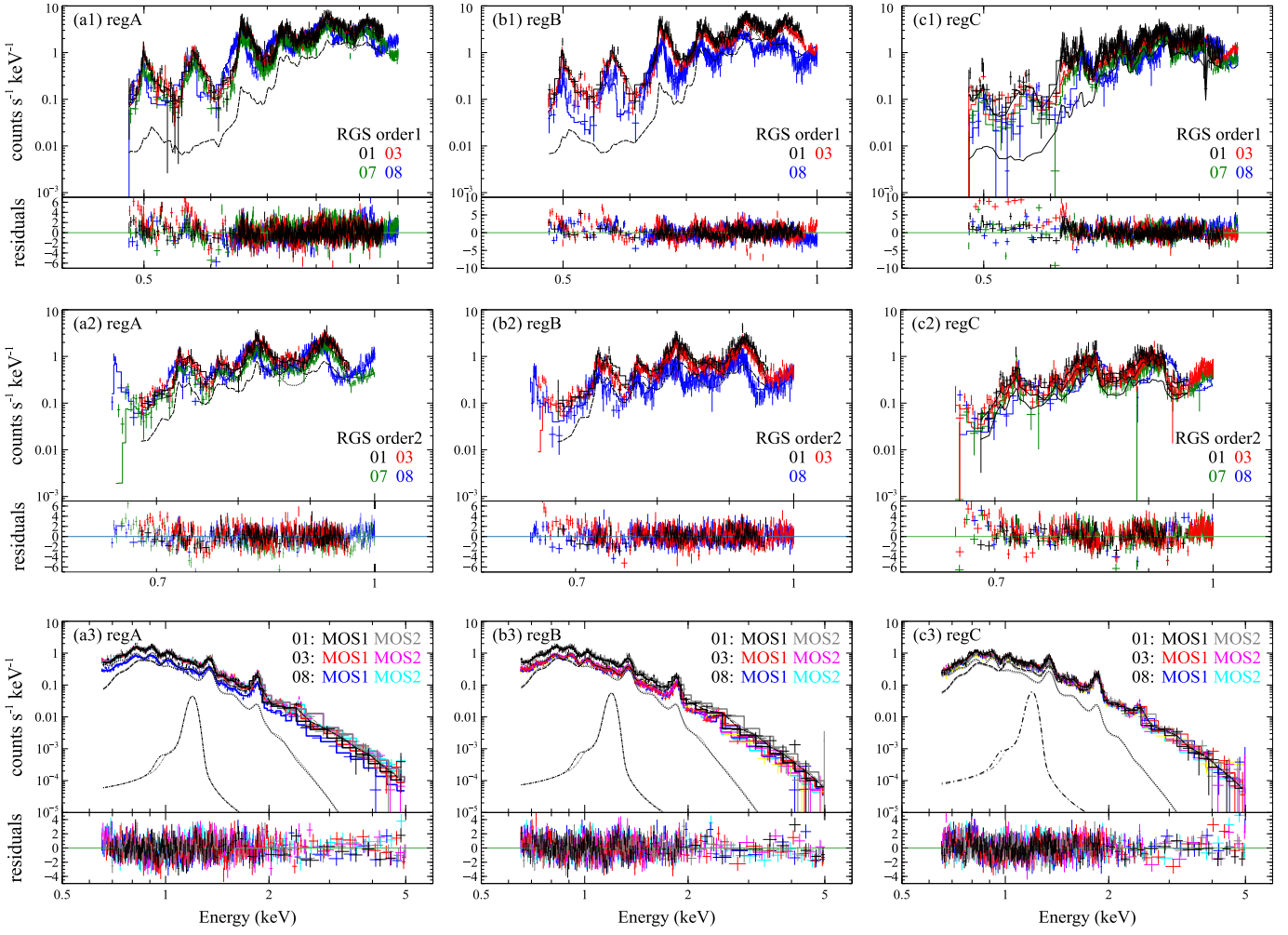
Figure 4. X-ray spectra of all the selected regions. Left: spectra of region A obtained with the first-order (a1) and second-order (a2) of RGS1+2 and those of MOS1/2 (a3). The numbers 01, 03, 07, and 08 represent the observation IDs 0113050601, 0302390101, 0743750201, and 0805050101, respectively. The dashed and dotted lines are the best-fit NEI components with high and low kT_e, respectively. The dotted–dashed lines show the Gaussian component (see text). Middle and right: the same as the left but spectra of regions B and C.

Table 2
Best-fit Parameters of the Spectrum

| Component	Parameter (Unit)	Region A	Region B	Region C
Absorption	N_H (10^{22} cm^{-2})	$0.881^{+0.002}_{-0.004}$	0.91 ± 0.01	1.07 ± 0.01
Low-temperature NEI	kT_e (keV)	$0.202^{+0.003}_{-0.001}$	0.200 ± 0.001	0.198 ± 0.002
(CSM)	N	1.4 ± 0.1	1.5 ± 0.1	$1.1^{+0.2}_{-0.3}$
	O	0.38 ± 0.01	$0.42^{+0.03}_{-0.01}$	$0.33^{+0.02}_{-0.03}$
	Ne	$0.62^{+0.01}_{-0.02}$	0.65 ± 0.02	$0.57^{+0.05}_{-0.01}$
	$n_e t$ (10^{11} cm^{-3} s)	>100	>100	>100
	norm	$1.23^{+0.05}_{-0.04}$	$1.31^{+0.07}_{-0.13}$	$0.51^{+0.06}_{-0.03}$
High-temperature NEI	kT_e (keV)	$0.650^{+0.003}_{-0.007}$	0.59 ± 0.01	0.57 ± 0.01
(ejecta)	Ne	2.0 ± 0.1	$1.8^{+0.6}_{-0.2}$	1.2 ± 0.1
	Mg	1.5 ± 0.1	$1.5^{+0.4}_{-0.1}$	$1.4^{+0.2}_{-0.1}$
	Si	$2.2^{+0.1}_{-0.2}$	2.0 ± 0.2	$1.9^{+0.2}_{-0.1}$
	S	$1.3^{+0.2}_{-0.1}$	1.4 ± 0.2	$1.3^{+0.2}_{-0.1}$
	Fe (= Ni)	$1.48^{+0.2}_{-0.3}$	$1.6^{+0.2}_{-0.1}$	1.3 ± 0.1
	$n_e t$ (10^{11} cm^{-3} s)	$3.2^{+0.4}_{-0.2}$	$5.0^{+1.7}_{-0.3}$	$3.7^{+0.3}_{-0.7}$
	norm	$0.044^{+0.003}_{-0.002}$	0.055 ± 0.005	0.023 ± 0.002
	W-statistic/d.o.f.	20,769/15,339	13,992/12,746	15,517/15,340
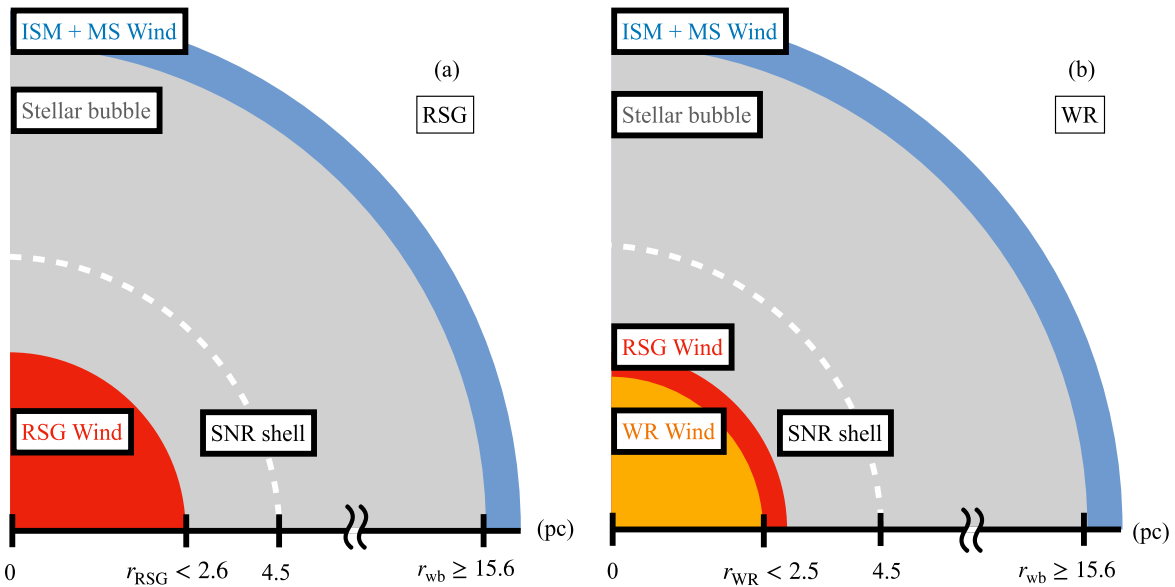
Figure 5. Schematic view of the environment around a star at the end of its life. (a) A low-mass star ends up as an RSG. Colors correspond to the shell of ISM and MS winds (blue), the stellar bubble (gray), and RSG winds (red). The white dashed line represents the position of the forward shock of RCW 103. (b) A massive star ends its life as a WR. The region dominated by a WR wind is represented in orange.

the H-burning layer of stars with $M_{ZAMS} = 10–12\,M_\odot$ are carried to the stellar surface by convection at an earlier stage of evolution than those of more massive stars: for instance, in the case of $M_{ZAMS} \sim 15\,M_\odot$, the He-burning occurs before the RSG phase, which prevents the star's expansion resulting in an inefficient transfer of N to the stellar surface.

As claimed by previous studies (Heger et al. 2000; Owocki 2004), rotation velocities of stars also affect the final yield of the CNO elements. This is clearly seen, for instance, in Figures 6(b1) and (b2), where N/O increases more rapidly as a result of faster rotation ($v_{init}/v_K = 0.1$, where v_{init} is the initial surface rotation velocity and v_K is the Kepler velocity at the surface). The trend is interpreted as an effect of centrifugal force, which enhances the mass-loss rate at the stage of OB stars (Owocki 2004) and carries materials such as C and O from the He-burning layer to the H-burning layer, causing additional N production by the CNO cycle (Heger et al. 2000).

We also investigate the effect of the convective overshoots, which may also enhance the abundance ratio of N/O because convective layers contain a large amount of N-rich materials (e.g., Luo et al. 2022). In the HOSHI code, convective overshoot is treated as a diffusion approximation with the diffusion coefficient $D = D_0 \exp(-2\Delta r/f_{ov} H_p)$, where D_0 is the diffusion constant at the boundary, Δr is the distance from the boundary, f_{ov} is the overshoot parameter variable, and H_p is the pressure scale height. We tried two overshoot models with different variables ($f_{ov} = 0.01$ and 0.03, namely models M_A and L_A, respectively, given in Section 2 of Luo et al. 2022) and found that a higher overshoot parameter results in a higher N/O on the stellar surface as seen in Figures 6(b1) and (b3). This is because N-rich materials in the H-burning layer are carried to the region closer to the surface by convection.

4.3. Progenitor Constraint with N/O

In accordance with the calculations demonstrated in Section 4.2, we compared the measured abundance ratio of N/O = 3.8 ± 0.1 in the CSM of RCW 103 with several models having different M_{ZAMS}, rotation velocities, and overshoot

parameters. In this analysis, we calculated the abundance ratio of N/O by summing up the total amount of N and O contained in post-main-sequence winds. The abundance evolution of WR stars and RSGs was obtained from the results in Ekström et al. (2012) and the model calculations using the Hoshi code, respectively. The results are displayed in Figure 7 (WR) and Figure 8 (RSG), from which we can constrain the progenitor properties and the origin of RCW 103.

If we assume the WR models, the progenitor of RCW 103 is likely to be a 25–32 $M_\odot$ star with a very rapid initial rotation velocity ($v_{init}/v_{crit} = 0.4$, where v_{crit} is the critical velocity reached when the gravitational acceleration is equal to the centrifugal force in the Roche model) or a 40–50 $M_\odot$ star with no rotation. Here, it is noted that v_{crit} differs slightly from v_K by a factor of $\sqrt{2/3}$. These results, however, are inconsistent with recent theoretical expectations that stars over 20 $M_\odot$ are hard to explode and that those over 35 $M_\odot$ mostly become black holes (Sukhbold et al. 2016). Although the explodability of such massive stars is under debate, we conclude that it is less likely that the progenitor of RCW 103 was a WR star.

In the case of an RSG (Figure 8), the progenitor of RCW 103 is likely to be a low-mass ($\leqslant 12\,M_\odot$) or medium-mass ($\geqslant 15\,M_\odot$) star with normal rotation velocities ($v_{init}/v_K \leqslant 0.2$). The latter result is consistent with a previous estimation based on the ejecta abundances ($\sim 18\,M_\odot$; Frank et al. 2015). However, this is somewhat unlikely in the context of birth conditions of compact objects (Higgins & Vink 2019). They present a relation between the progenitor properties and a compactness parameter ζ_M, which is defined as

$$\zeta_M = \left.\frac{M/M_\odot}{R(M_{bary} = M)/1000\ \text{km}}\right|_{t=t_{bounce}}, \qquad (4)$$

where M is the relevant mass scale for black hole formation and $R(M_{bary} = M)$ is the radial coordinate that encloses M at the time of core bounce (O'Connor & Ott 2011). Higgins & Vink (2019) claimed that ζ_M is related to how easily a pre-supernova stellar core explodes. As they suggest, it is difficult for stars of medium
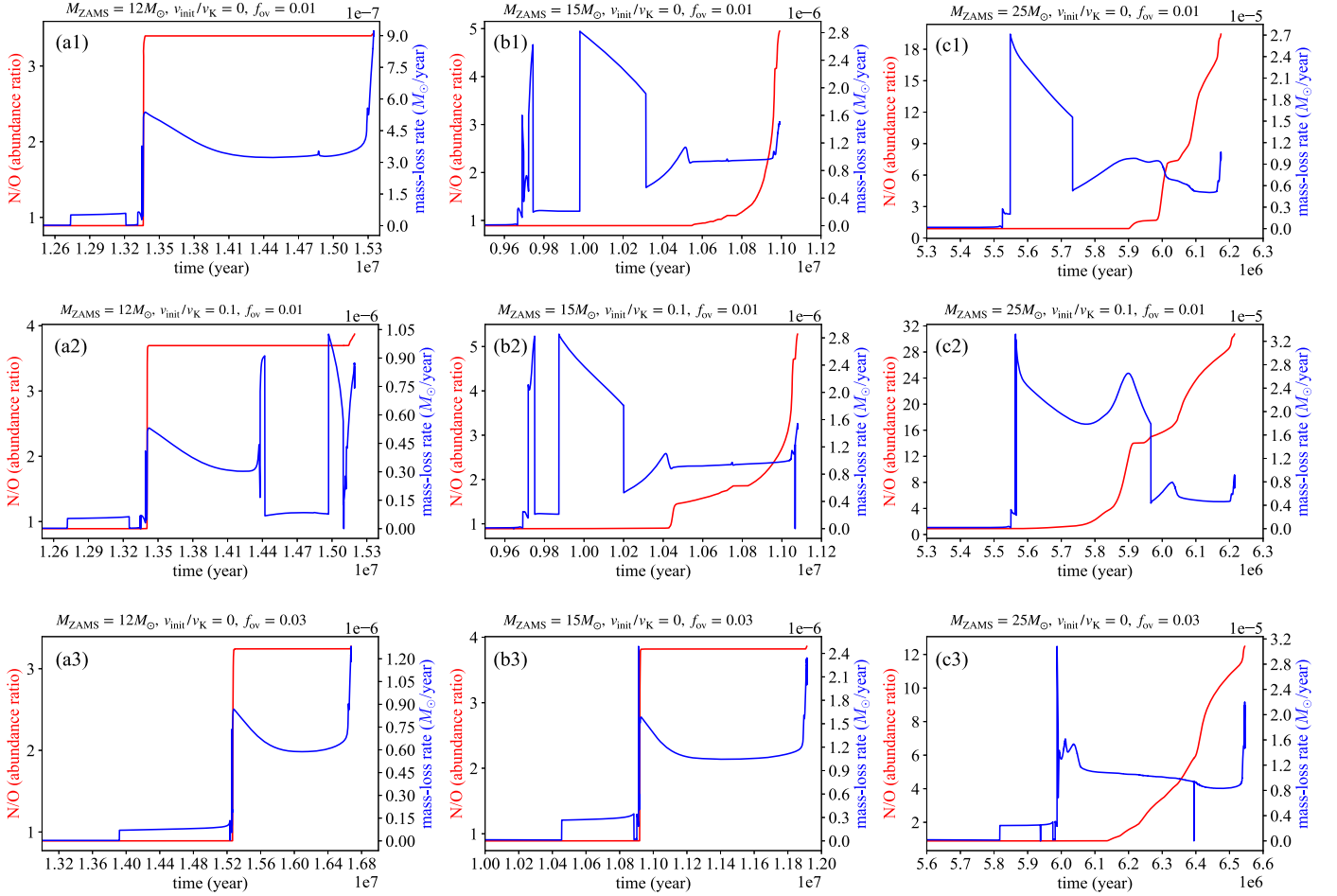
Figure 6. Relations between the time from the birth of stars and the abundance ratio N/O at the stellar surface (red) and the mass-loss rate (blue). Top: models with 12 $M_\odot$ (a1), 15 $M_\odot$ (b1), and 25 $M_\odot$ (c1), with no rotation and a low overshoot parameter ($f_{ov} = 0.01$). Middle: same as the top but the initial rotation velocity is higher ($v_{init}/v_K = 0.1$). Bottom: same as the top but the overshoot parameter is higher ($f_{ov} = 0.03$).

M_{ZAMS} (15–40 $M_\odot$) to explode except those that have very rapid rotation velocities ($v_{init}/v_K \geqslant 0.4$), which can be ruled out by our estimation (the black lines in Figure 8).

By contrast, low-mass (10–12 $M_\odot$) progenitor models are acceptable from the point of view of the explodability and also fit well with previous estimations derived from a comparison of metal compositions of ejecta with a core-collapse nucleosynthesis model: 12–13 $M_\odot$ (Braun et al. 2019) and <13 $M_\odot$ (Zhou et al. 2019). We also point out that according to the relation between Fe/Si and M_{ZAMS} given by Katsuda et al. (2018) the obtained ejecta abundance ratio (Fe/Si > 0.6 from Table 2) prefers a lower-mass star as well. From these results, we conclude that the progenitor of RCW 103 was most likely a star with M_{ZAMS} of 10–12 $M_\odot$. We also presume that its rotation velocity was relatively normal: $v_{init}/v_K \leqslant 0.2$.

4.4. Origin of the Magnetar and Future Perspectives

RCW 103 has a magnetar candidate 1E 161348−5055. Our result may also hint at physical conditions that lead to the formation of magnetars after SN explosions. One of the well-established hypotheses is a "dynamo effect" model (Thompson & Duncan 1993). In this scenario, magnetars are born with rapidly rotating (of the order of milliseconds) proto-neutron stars (PNSs), which can power energetic SNe (or release most of the energy through gravitational waves).

Since the rotation velocity of PNSs shows a positive correlation with M_{ZAMS}, Gaensler et al. (2005) and Heger et al. (2005) indicate that fairly high M_{ZAMS} ($\geqslant 35 M_\odot$) is required to produce a magnetar with this effect in the case of progenitors with $v_{init} = 200\,\mathrm{km\,s^{-1}}$. On the other hand, White et al. (2022) suggest that low-mass progenitors ($M_{ZAMS} = 9$–25 $M_\odot$) with no initial rotation can also create strong magnetic fields by the dynamo effect considering sufficiently low Rossby number. Masada et al. (2022) also suggest that strong magnetic fields can be generated in relatively slowly ($\sim 100\,\mathrm{ms}$) rotating PNSs considering different internal structures of the convection. From Figure 7, there is no possible solution for $\geqslant 35 M_\odot$ with a rapid rotation ($v_{init} > 300\,\mathrm{km\,s^{-1}}$), and the progenitor parameters given by White et al. (2022) are consistent with our estimation. An alternative scenario to account for the formation of the magnetars is the fossil field hypothesis, which requires a progenitor star with strong magnetic fields (Ferrario & Wickramasinghe 2006; Vink & Kuiper 2006; Hu & Lou 2009) originating from massive (>20 $M_\odot$; Ferrario & Wickramasinghe 2006, 2008) or less massive progenitors (Hu & Lou 2009). This case is also in good agreement with our estimation and it is consistent with the previous study (Zhou et al. 2019).

Note that 1E 161348−5055 has an extremely long period (6.67 hr; De Luca et al. 2006) unlike most magnetars (~ 1–10 s; Olausen & Kaspi 2014). Some magnetars with short periodicity
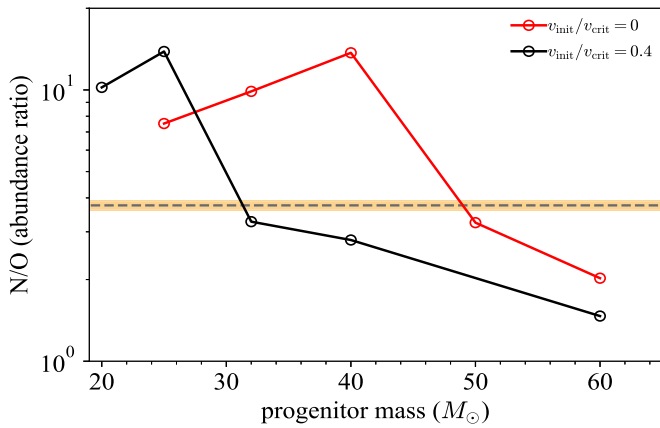
Figure 7. Measured N/O from our observation (the orange shaded region) and those expected in the swept-up CSM with different M_{ZAMS} calculated with Geneva code (the red and black circles). The black dashed horizontal line and the width show the averaged N/O in RCW 103 and its 1σ errors, respectively. The red and black circles correspond to cases of $v_{init}/v_{crit} = 0$ and 0.4, respectively.
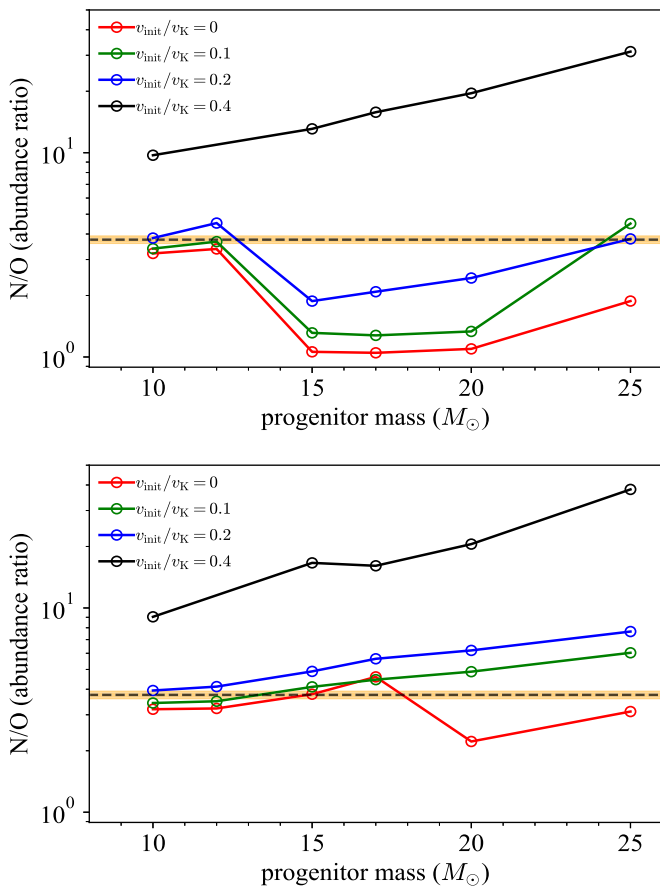

Figure 8. Same as Figure 7 but for the RSG models calculated with the HOSHI code. Colors correspond to different rotation velocities: $v_{init}/v_K = 0$ (red), 0.1 (green), 0.2 (blue), and 0.4 (black). Models with lower ($f_{ov} = 0.01$) and higher ($f_{ov} = 0.03$) overshoot parameters are displayed in the top and bottom panels, respectively.

are thought to have low-mass progenitors (Zhou et al. 2019) and many OB stars in our Galaxy have the same velocity as the progenitor of RCW 103 (Daflon et al. 2007). Therefore, the progenitor of RCW 103 is thought to have similar physical characteristics to the majority of OB stars in our Galaxy except for the extremely long period of 1E 161348−5055.

A measurement of N/O in CSM established in our study is a good method to constrain progenitors of SNRs; e.g., stellar properties such as M_{ZAMS}, initial rotation velocities, and convective overshoots. The microcalorimeter Resolve on board the XRISM satellite (Tashiro et al. 2018) will be able to detect the C, N, and O lines in many diffuse sources in our Galaxy. Athena (Barret et al. 2018) and Lynx (Gaskin et al. 2019) will be able to expand the targets to SNRs in the Large and Small Magellanic Clouds. With these future observatories, measurement of the CNO abundances will become a key method to probe the relationship between stellar evolution and the final fate of stars, such as supernovae and compact objects, and the probability of formation of magnetars, neutron stars, and black holes.

5. Conclusions

We performed high-resolution spectroscopy of RCW 103 with the RGS on board XMM-Newton and detected N VII Lyα (0.50 keV) for the first time. All the spectra are well reproduced by a two-component NEI model with different temperatures. The obtained value of N/O $= 3.8 \pm 0.1$ indicates the presence of shock-heated CSM and thus we investigated RCW 103's progenitor parameters such as M_{ZAMS}, rotation velocity, and overshoot parameters by using the stellar evolution codes HOSHI and Geneva. As a result, we successfully constrained the progenitor of RCW 103 as a low-mass star ($M_{ZAMS} = 10$–$12\ M_\odot$) with a relatively normal rotation velocity ($v_{init}/v_K \leqslant 0.2$). Consequently, the dynamo effect and the fossil field are plausible for the origin of the associated magnetar 1E 161348−5055, and we conclude that the progenitor of RCW 103 is similar to the majority of OB stars while the extremely long period of 1E 161348−5055 is still an open question. Our method will become a useful tool for constraining progenitor properties of Galactic and extragalactic SNRs with future microcalorimeter missions such as XRISM, Athena, and Lynx.

ORCID iDs

Takuto Narita https://orcid.org/0009-0006-7889-6144
Hiroyuki Uchida https://orcid.org/0000-0003-1518-2188
Takashi Yoshida https://orcid.org/0000-0002-8967-7063
Takaaki Tanaka https://orcid.org/0000-0002-4383-0368
Takeshi Go Tsuru https://orcid.org/0000-0002-5504-4903

References

Arnaud, K. A. 1996, in ASP Conf. Ser. 101, Astronomical Data Analysis Software and Systems V, ed. G. H. Jacoby & J. Barnes (San Francisco, CA: ASP), 17
Barret, D., Lam Trong, T., den Herder, J.-W., et al. 2018, Proc. SPIE, 10699, 106991G
Berghöfer, T. W., Bowyer, S., Lieu, R., & Knude, J. 1998, ApJ, 500, 838
Braun, C., Safi-Harb, S., & Fryer, C. L. 2019, MNRAS, 489, 4444
Carter, L. M., Dickel, J. R., & Bomans, D. J. 1997, PASP, 109, 990
Castor, J., McCray, R., & Weaver, R. 1975, ApJL, 200, L107

Chen, Y., Zhou, P., & Chu, Y.-H. 2013, ApJL, 769, L16
Chevalier, R. A. 1999, ApJ, 511, 798
Chevalier, R. A. 2005, ApJ, 619, 839
Chevalier, R. A., & Emmering, R. T. 1989, ApJL, 342, L75
Chevalier, R. A., & Imamura, J. N. 1983, ApJ, 270, 554
Daflon, S., Cunha, K., de Araújo, F. X., Wolff, S., & Przybilla, N. 2007, AJ, 134, 1570
De Luca, A., Caraveo, P. A., Mereghetti, S., Tiengo, A., & Bignami, G. F. 2006, Sci, 313, 814
Dwarkadas, V. V. 2005, ApJ, 630, 892
Dwarkadas, V. V. 2007, ApJ, 667, 226
Ekström, S., Georgy, C., Eggenberger, P., et al. 2012, A&A, 537, A146
Ferrario, L., & Wickramasinghe, D. 2006, MNRAS, 367, 1323
Ferrario, L., & Wickramasinghe, D. 2008, MNRAS Lett., 389, L66
Frank, K. A., Burrows, D. N., & Park, S. 2015, ApJ, 810, 113
Gaensler, B. M., McClure-Griffiths, N. M., Oey, M. S., et al. 2005, ApJL, 620, L95
Gaskin, J. A., Swartz, D. A., Vikhlinin, A., et al. 2019, JATIS, 5, 021001
Goldman, S. R., van Loon, J. T., Zijlstra, A. A., et al. 2017, MNRAS, 465, 403
Heger, A., Langer, N., & Woosley, S. E. 2000, ApJ, 528, 368
Heger, A., Woosley, S. E., & Spruit, H. C. 2005, ApJ, 626, 350
Higgins, E. R., & Vink, J. S. 2019, A&A, 622, A50
Hu, R.-Y., & Lou, Y.-Q. 2009, MNRAS, 396, 878
Kasuga, T., Vink, J., Katsuda, S., et al. 2021, ApJ, 915, 42
Katsuda, S., Takiwaki, T., Tominaga, N., Moriya, T. J., & Nakamura, K. 2018, ApJ, 863, 127
Luo, T., Umeda, H., Yoshida, T., & Takahashi, K. 2022, ApJ, 927, 115
Maeder, A. 1983, A&A, 120, 113
Maeder, A., Przybilla, N., Nieva, M.-F., et al. 2014, A&A, 565, A39
Masada, Y., Takiwaki, T., & Kotake, K. 2022, ApJ, 924, 75

Mauron, N., & Josselin, E. 2011, A&A, 526, A156
O'Connor, E., & Ott, C. D. 2011, ApJ, 730, 70
Okon, H., Tanaka, T., Uchida, H., et al. 2020, ApJ, 890, 62
Olausen, S. A., & Kaspi, V. M. 2014, ApJS, 212, 6
Owocki, S. 2004, in EAS Publications Series, ed. M. Heydari-Malayeri, P. Stee, & J. P. Zahn, Vol. 13 (Les Ulis: EDP Sciences), 163
Przybilla, N., Firnstein, M., Nieva, M. F., Meynet, G., & Maeder, A. 2010, A&A, 517, A38
Reynoso, E. M., Green, A. J., Johnston, S., et al. 2004, PASA, 21, 82
Sapienza, V., Miceli, M., Bamba, A., et al. 2022, ApJ, 935, 152
Smartt, S. J. 2009, ARA&A, 47, 63
Sukhbold, T., Ertl, T., Woosley, S. E., Brown, J. M., & Janka, H. T. 2016, ApJ, 821, 38
Takahashi, K., Umeda, H., & Yoshida, T. 2014, ApJ, 794, 40
Takahashi, K., Yoshida, T., & Umeda, H. 2013, ApJ, 771, 28
Takahashi, K., Yoshida, T., & Umeda, H. 2018, ApJ, 857, 111
Takahashi, K., Yoshida, T., Umeda, H., Sumiyoshi, K., & Yamada, S. 2016, MNRAS, 456, 1320
Tashiro, M., Maejima, H., Toda, K., et al. 2018, Proc. SPIE, 10699, 1069922
Thompson, C., & Duncan, R. C. 1993, ApJ, 408, 194
Uchida, H., Katsuda, S., Tsunemi, H., et al. 2019, ApJ, 871, 234
Vink, J., & Kuiper, L. 2006, MNRAS Lett., 370, L14
Wachter, K., Leach, R., & Kellogg, E. 1979, ApJ, 230, 274
Weaver, R., McCray, R., Castor, J., Shapiro, P., & Moore, R. 1977, ApJ, 218, 377
White, C. J., Burrows, A., Coleman, M. S. B., & Vartanyan, D. 2022, ApJ, 926, 111
Wilms, J., Allen, A., & McCray, R. 2000, ApJ, 542, 914
Yoshida, T., Takiwaki, T., Kotake, K., et al. 2019, ApJ, 881, 16
Zhou, P., Vink, J., Safi-Harb, S., & Miceli, M. 2019, A&A, 629, A51